Electronic Supporting Information

Tandem templating strategies facilitate the assembly of calix[8]arene-supported Ln_{18} clusters

Yushu Jiao,[a] Sergio Sanz,*[b], Jan van Leusen,[a] David Gracia,[c] Angelos B. Canaj,[d] Marco Evangelisti,*[c] Euan K. Brechin,*[d] Scott J. Dalgarno*[e] and Paul Kögerler*[a,b]

a. Institute of Inorganic Chemistry, RWTH Aachen University, 52056 Aachen, Germany. E-mail: paul.koegerler@ac.rwth-aachen.de
b. Peter Grünberg Institute 6, Forschungszentrum Jülich, 52425 Jülich, Germany. E-mail: s.calvo@fz-juelich.de
c. Instituto de Nanociencia y Materiales de Aragón (INMA), CSIC – Universidad de Zaragoza, Departamento de Física de la Materia Condensada, 50009 Zaragoza, Spain. E-mail: evange@unizar.es
d. EaStCHEM School of Chemistry, The University of Edinburgh, David Brewster Road, Edinburgh, EH9 3FJ, UK. E-mail: ebrechin@ed.ac.uk
e. Institute of Chemical Sciences, Heriot-Watt University, Riccarton, Edinburgh, EH14 4AS, UK. E-mail: S.J.Dalgarno@hw.ac.uk

Contents

I. Instrumentation

Infrared spectra were collected on a Bruker VERTEX 70 FT-IR spectrometer coupled with a RAM II FT-Raman module. UV–Vis spectra were measured on a Shimadzu UV–2600 spectrophotometer (10 mm quartz glass cuvettes for liquid-state samples) at room temperature. CHN Elemental Analyses were analyzed in an Elementar VarioEL. Powder X-ray diffraction data were collected on a STADI P powder diffractometer from STOE using a Cu-Kα radiation (λ = 1.54059 Å) and a focusing Ge monochromator (Johann-type) at room temperature. Thermogravimetric thermal analyses were performed on a Mettler Toledo SDTA 851 under air at a heating rate of 1 K min^{-1}.

II. IR details of Ln_2 complexes

La_2

IR ($\tilde{\nu}$ / cm^{-1}): 2957 (m), 2907 (w), 2866 (w), 1635 (w), 1480 (vs), 1391 (m), 1360 (m), 1298 (s), 1261 (w), 1205 (w), 1122 (w), 1099 (w), 1022 (m), 962 (s), 908 (w), 870 (w), 819 (vs), 748 (w), 649 (m), 566 (w), 528 (w).

Nd_2

IR ($\tilde{\nu}$ / cm^{-1}): 2957 (m), 2907 (w), 2866 (w), 1635 (w), 1480 (vs), 1391 (m), 1360 (m), 1298 (s), 1261 (w), 1205 (w), 1122 (w), 1099 (w), 1022 (m), 962 (s), 908 (w), 870 (w), 819 (vs), 748 (w), 649 (m), 566 (w), 528 (w).

Gd_2

IR ($\tilde{\nu}$ / cm^{-1}): 2953 (m), 2907 (w), 2865 (w), 1603 (w), 1483 (vs), 1391 (m), 1360 (m), 1296 (w), 1207 (w), 1124 (w), 1020 (m), 961 (s), 911 (w), 870 (w), 821 (vs), 750 (w), 667 (m), 528 (w).

III. Coordination geometry of La^{III} ions in La^{III}_{18}

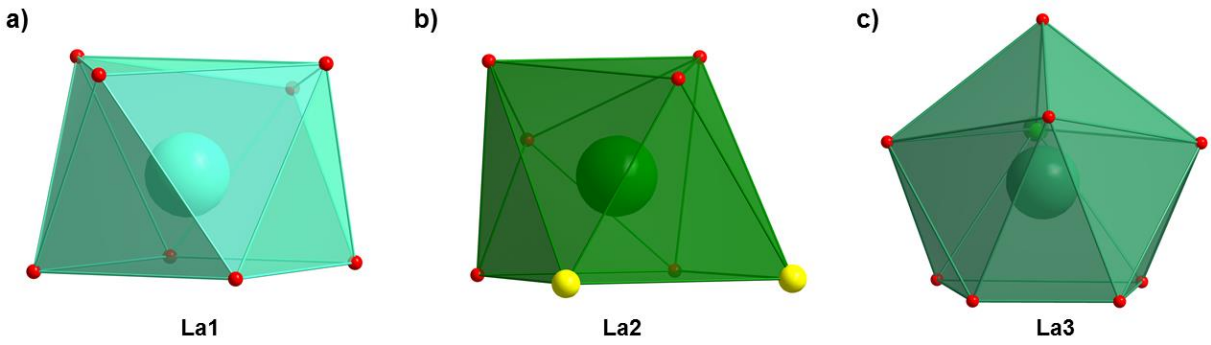

Fig. S1. a) Distorted square antiprismatic $Ln^{III}O_8$ geometry in La1 ions. b) Distorted square antiprismatic $Ln^{III}O_6Cl_2$ geometry in La2 ions. c) Distorted capped square antiprismatic $Ln^{III}O_8Cl$ geometry in La3 ions. Colour code: La1 = cyan, La2 = green, La3 = pale green, O = red, and Cl = yellow.

IV. Additional SCXRD information

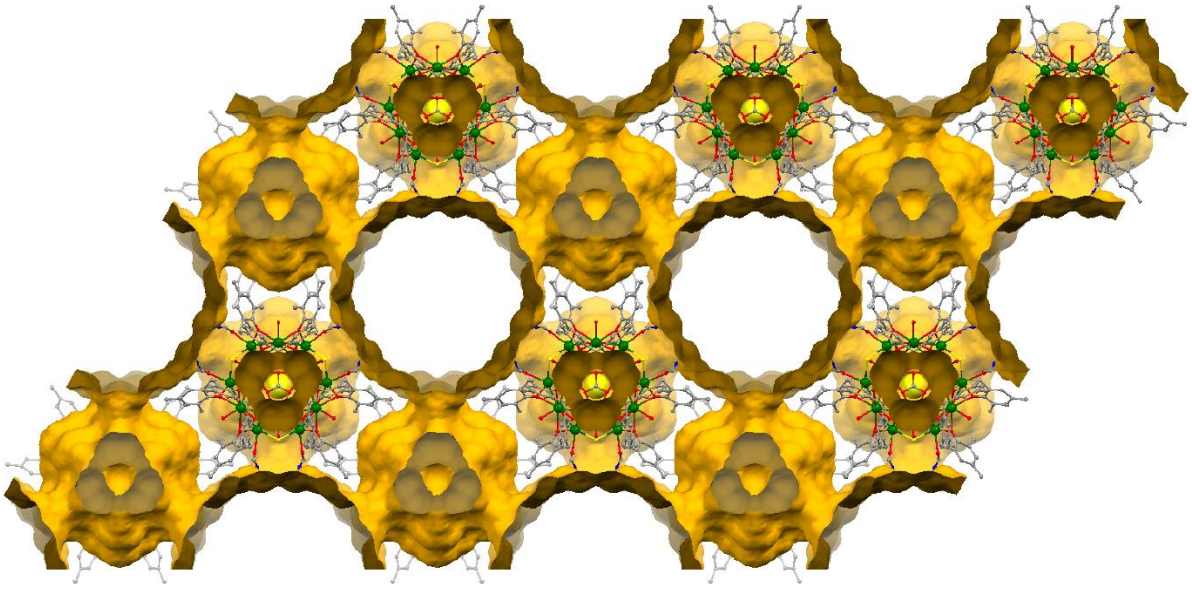

Fig. S2. Crystal packing of **1** view along the *c* axis. The empty space calculation by using the void calculation tool in Mercury 2022.3 for a spherical probe radius of 1.5 Å and a grid spacing of 0.3 Å accounts for ~50% of its volume. The available space is represented in white color.

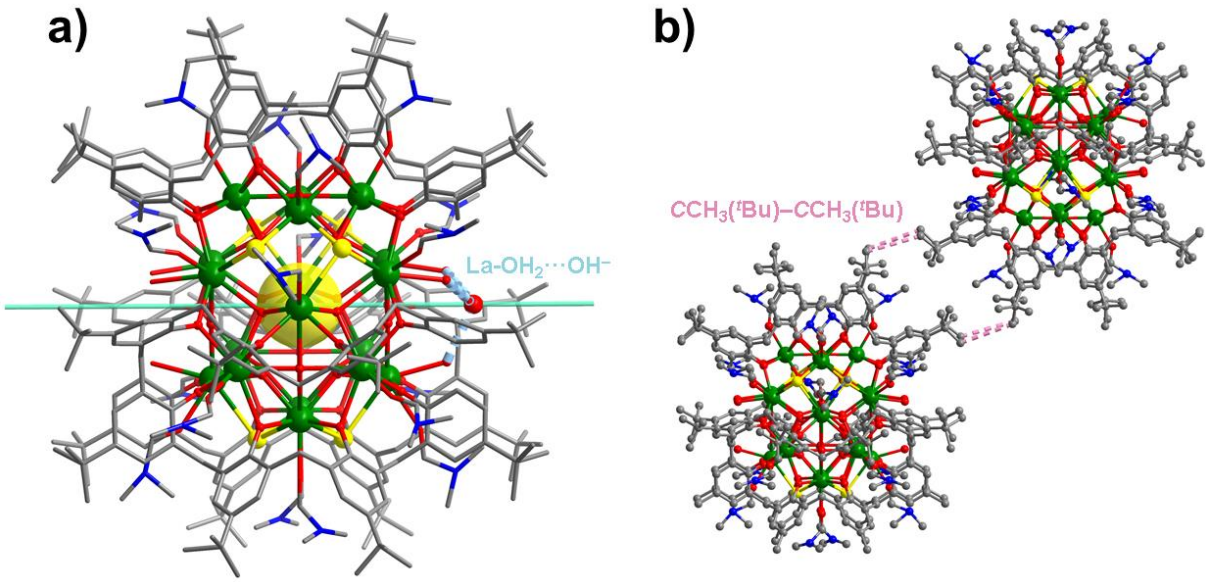

Fig. S3. a) Molecular structure of $[La^{III}_{18}(TBC[8]\text{-}8H)_3(\mu_4\text{-}O)_3(\mu_3\text{-}Cl)_6(\mu_3\text{-}OH)_{12}(\mu_3\text{-}CO_3)_2(H_2O)_6(DMF)_{18}Cl]OH\cdot H_2O\cdot 12DMF$ with the C_3 axis passing through the two central carbon atoms of the two carbonate ligands, the central Cl^- anion, and the OH^- counteranion, showing the hydrogen bonding interaction of La-$OH_2\cdots OH^-$ at 2.599 Å distance. b) The intermolecular $CCH_3(^tBu)$–$CCH_3(^tBu)$ interactions between neighboring molecules. Color code: La: green, O: red, Cl: yellow, N: blue, and C: gray.

Table S1. Crystallographic data and structure refinement details for **1**.

Compound	**1**
CCDC	2299004
Radiation type	Cu Kα
Empirical formula	$C_{356}H_{549}Cl_7La_{18}N_{30}O_{83}$
Formula weight / g mol^{-1}	9325.75
Crystal system	Trigonal
Space group	*P*-31*c*
a / Å	32.5846(4)
b / Å	32.5846(4)
c / Å	34.4461(6)
α	90°
β	90°
γ	120°
Volume / Å^3	31673.5(10)
Z	2
D_{calc} / g cm^{-3}	0.978
Absorption coefficient / mm^{-1}	9.799
F (000)	9408
Crystal size / mm^3	0.4×0.24×0.08
Theta range for data collection	6.264–130.688°
Completeness to Θ_{max}	99.7 %
Index ranges	$-37 \le h \le 38$, $-38 \le k \le 37$, $-40 \le l \le 40$
Reflections collected	458160
Independent reflections	18091
R_{int}	0.1166
Observed ($I > 2\sigma(I)$)	8437
Absorption correction	Multi-scan
T_{min}/T_{max}	0.3649/0.7516
Data/restraints/parameters	18091/470/852
Goodness-of-fit on F^2	1.103
R_1, wR_2 ($I > 2\sigma(I)$)	R_1 = 0.0832, wR_2 = 0.2445
R_1, wR_2 (all data)	R_1 = 0.1262, wR_2 = 0.3071
Largest diff. peak and hole / e Å^{-3}	1.05 / –1.12

Table S2. Unit cell parameters for **2** and **3**.

Compound	**2**	**3**
Radiation type	Cu Kα	Cu Kα
Empirical formula	$C_{320}H_{465}Cl_7Nd_{18}N_{18}O_{71}$	$C_{320}H_{465}Cl_7Gd_{18}N_{18}O_{71}$
Molecular weight / g mol^{-1}	8544.80	8778.95
Crystal system	Trigonal	Trigonal
Space group	*P*-31*c*	*P*-31*c*
a / Å	32.306(0)	32.599(2)
b / Å	32.306(0)	32.599(2)
c / Å	34.250(4)	33.717(3)
α	90°	90°
β	90°	90°
γ	120°	120°
Volume / $Å^3$	30957.3(1)	31030.5(0)
Z	2	2
Crystal size / mm^3	0.07×0.07×0.27	0.05×0.05×0.16

Table S3. Selected bond lengths in **1**.

Bond Type	**Bond Length / Å**
La1–μ_2-O (TBC[8])	2.421–2.598
La1–μ_4-O	2.553
La1–μ_3-**O**H	2.546 and 2.553
La1–O_{DMF}	2.407
La2–μ_2-O (TBC[8])	2.404 and 2.405
La2–μ_4-O	2.827
La2–μ_3-OH	2.432 and 2.440
La2–O_{DMF}	2.419
La2– μ_3-Cl	2.974
La3–μ_2-O (TBC[8])	2.491 and 2.509
La3–μ_3-OH	2.574 and 2.590
La3–μ_3-CO_3	2.620 and 2.622
La3–O_{DMF}	2.500
La3–O_{H2O}	2.541
La3– μ_3-Cl	3.060

Table S4. Bond valence sum values for different atoms of **1**.

Atoms	BVS value
La1	3.15
La2	3.20
La3	3.08
μ_2-O (TBC[8])	
O1	–2.18
O2	–2.18
O3	–2.19
O4	–2.03
μ_3-OH	
O7	–1.16
O13	–1.14
μ_3-Cl	
Cl10	–1.01

V. IR spectra

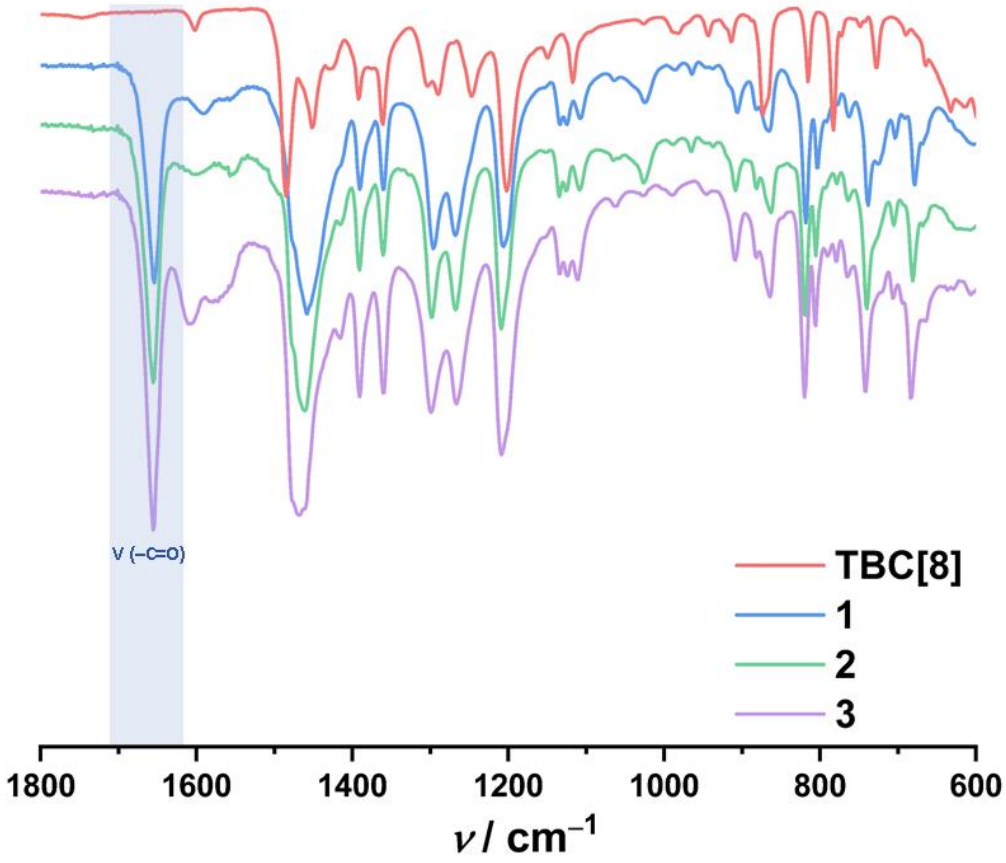

Fig. S4. IR spectra of TBC[8] (red line) and complexes **1**–**3** (**1**: blue; **2**: green; **3**: purple line).

VI. Powder X-ray diffraction

PXRD experiments of **1**–**3** were carried out at room temperature. Differences in the PXRD of samples **1**–**3** may be produced by the loss of crystallization solvent when crystals are collected from the mother liquor. Lower quality of the crystals results in a worsening of the experimental PXRD. Their lattice size variations at different temperatures contribute to the reflex position shifts between the experimental and theoretical curves, given that PXRD diffraction was performed at room temperature, while SXRD diffraction was performed at 100 K. The difference in the reflex intensity observed between the experimental and theoretical patterns could be attributed to the random orientation of the crystallites in the samples.

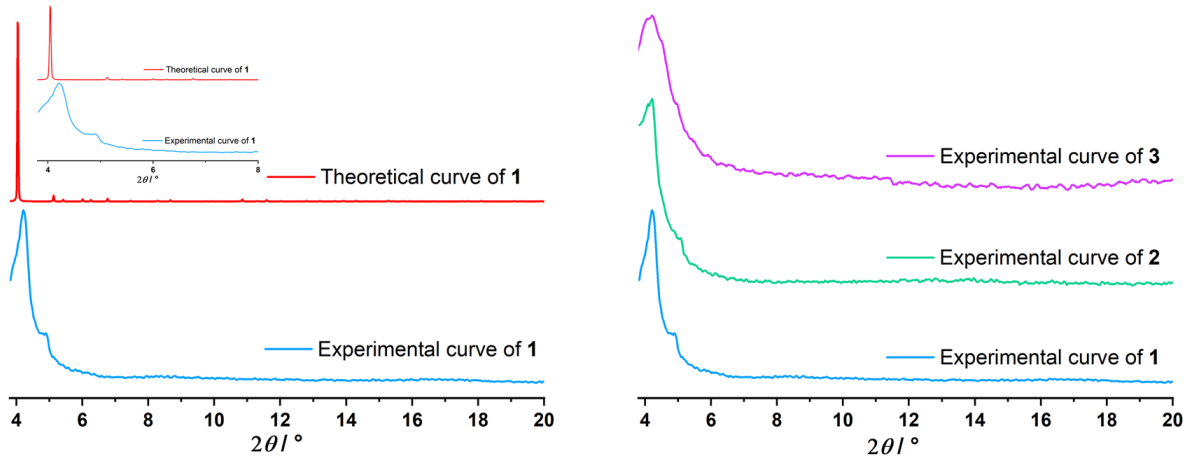

Fig. S5. Experimental and calculated (red line) PXRD patterns in the angles of 4–30° for **1** (blue), **2** (green), and **3** (purple line).

VII. UV-Vis spectroscopy

The liquid UV-Vis spectra (Fig. S6) of **1**–**3** in $CHCl_3$ solutions display similar characteristic bands. In the range of 800 – 250 nm, an absorption band can be observed at $\varepsilon = 2.27 \times 10^5$ (305 nm) $M^{-1}\,cm^{-1}$ for **1**; at 2.16×10^5 (304 nm) $M^{-1}\,cm^{-1}$ for **2**, and at 2.53×10^5 (304 nm) $M^{-1}\,cm^{-1}$ for **3**. These bands correspond to typical π-π* electronic transitions centered on the aromatic rings. Note that the UV-Vis curves of **3** are almost unchanged over a 24-hour period, indicating that these complexes do not decompose over the course of the measurements.

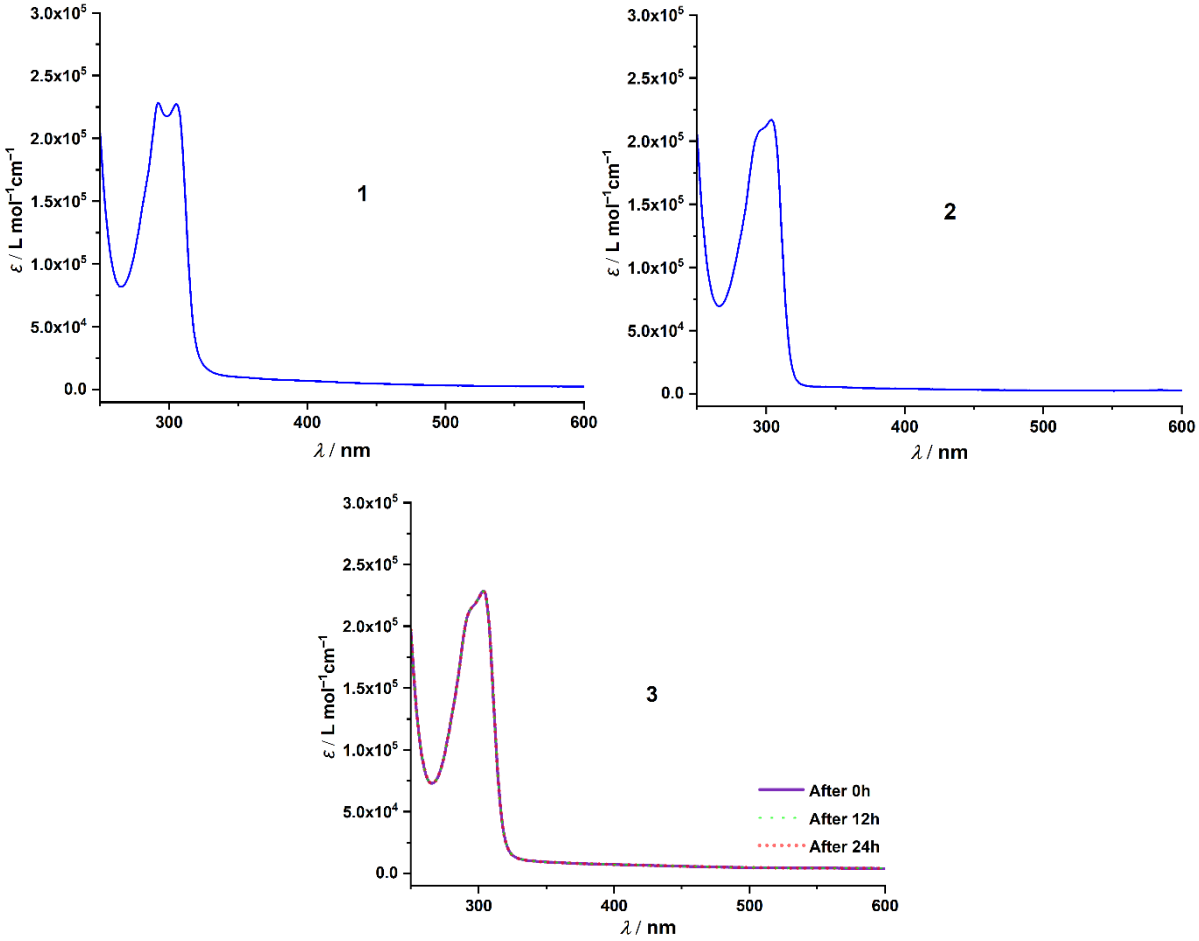

Fig. S6. UV-Vis spectra of **1**–**3** in $CHCl_3$ solutions.

VIII. Thermogravimetric analysis

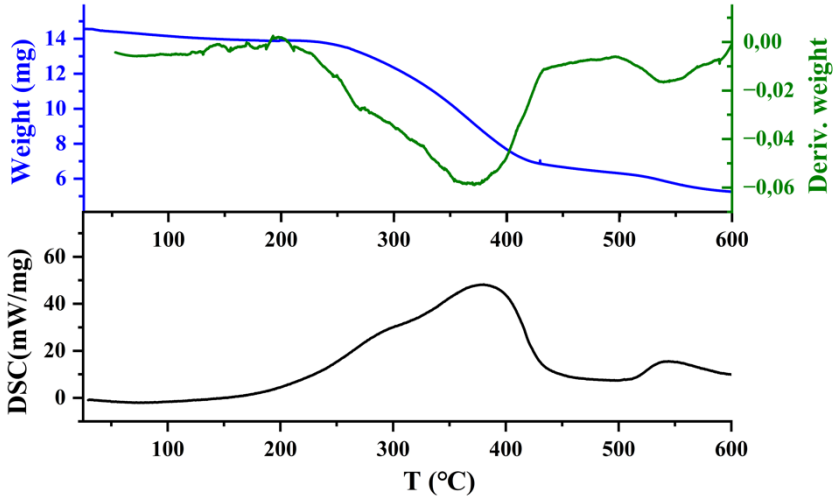

Fig. S7. TGA (blue line), weight derivative (green line), and DSC (black line) curves of **1**.

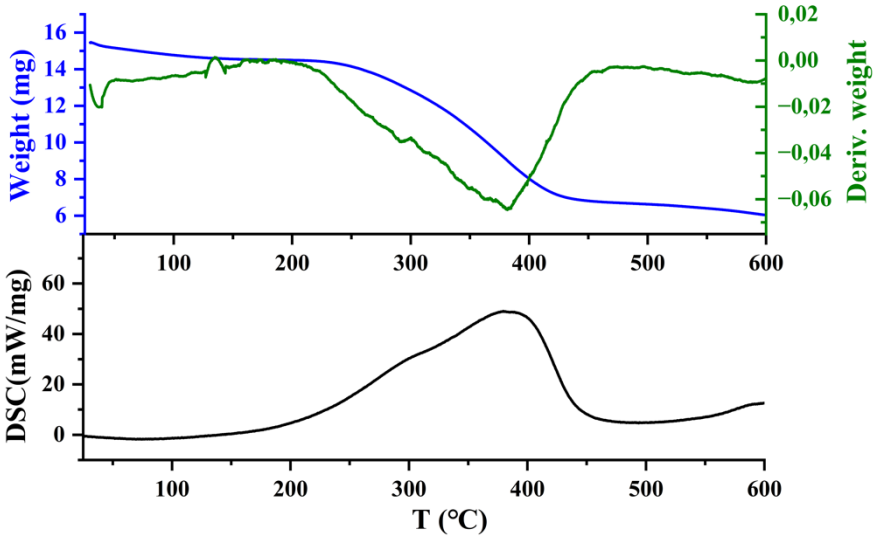

Fig. S8. TGA (blue line), weight derivative (green line), and DSC (black line) curves of **2**.

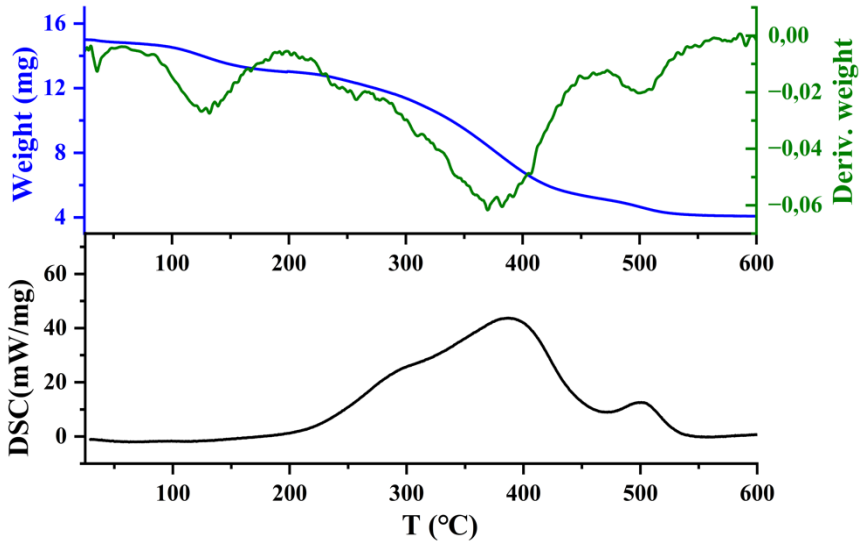

Fig. S9. TGA (blue line), weight derivative (green line), and DSC (black line) curves of **3**.

IX. Magnetocaloric studies

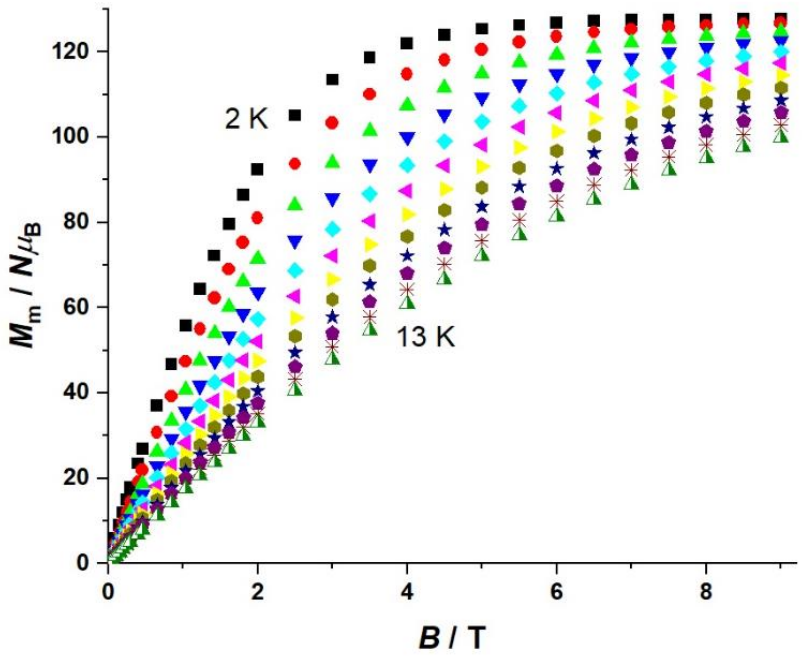

Fig. S10. Molar magnetization (M_m) vs. applied magnetic field (B) between 2 and 13 K, for **3**.

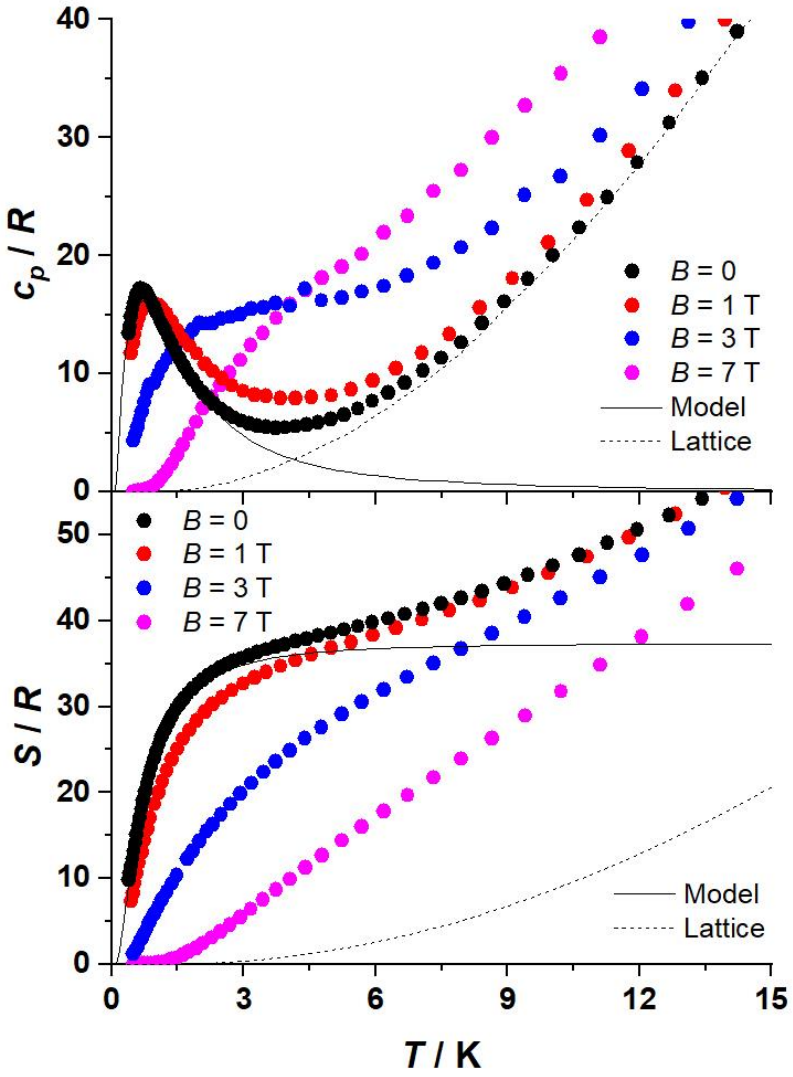

Fig. S11. Heat capacity (c_p, top) and entropy (S, bottom), normalized to the gas constant R, for **3** for selected applied field values, as labelled. The zero-field magnetic contributions to c_p and S are well described by the Schottky model for an effective field B_{eff} = 0.6 T (solid lines). The lattice contributions to c_p and S (dashed lines) are well accounted for by the Debye heat capacity, which simplifies to $c_{latt}/R = 4.1 \times 10^{-2}\ T^3$ at the lowest temperatures.